Characterization of the K2-19 Multiple-Transiting Planetary System via High-Dispersion Spectroscopy, AO Imaging, and Transit Timing Variations

Norio Narita[1,2,3], Teruyuki Hirano[4], Akihiko Fukui[5], Yasunori Hori[1,2], Roberto Sanchis-Ojeda[6,7], Joshua N. Winn[8], Tsuguru Ryu[2,3], Nobuhiko Kusakabe[1,2], Tomoyuki Kudo[9], Masahiro Onitsuka[2,3], Laetitia Delrez[10], Michael Gillon[10], Emmanuel Jehin[10], James McCormac[11], Matthew Holman[12], Hideyuki Izumiura[3,5], Yoichi Takeda[1], Motohide Tamura[1,2,13], Kenshi Yanagisawa[5]

norio.narita@nao.ac.jp

ABSTRACT

K2-19 (EPIC201505350) is an interesting planetary system in which two transiting planets with radii $\sim 7R_\oplus$ (inner planet b) and $\sim 4R_\oplus$ (outer planet c) have

[1]Astrobiology Center, 2-21-1 Osawa, Mitaka, Tokyo, 181-8588, Japan

[2]National Astronomical Observatory of Japan, 2-21-1 Osawa, Mitaka, Tokyo, 181-8588, Japan

[3]SOKENDAI (The Graduate University for Advanced Studies), 2-21-1 Osawa, Mitaka, Tokyo, 181-8588, Japan

[4]Department of Earth and Planetary Sciences, Tokyo Institute of Technology, 2-12-1 Ookayama, Meguro-ku, Tokyo 152-8551, Japan

[5]Okayama Astrophysical Observatory, National Astronomical Observatory of Japan, Asakuchi, Okayama 719-0232, Japan

[6]Department of Astronomy, University of California, Berkeley, CA 94720, USA

[7]NASA Sagan Fellow

[8]Department of Physics, and Kavli Institute for Astrophysics and Space Research, Massachusetts Institute of Technology, Cambridge, MA 02139, USA

[9]Subaru Telescope, 650 North A'ohoku Place, Hilo, HI 96720, USA

[10]Institut dAstrophysique et de Géophysique, Université de Liège, Allée du 6 Août 17, Bat. B5C, 4000 Liège, Belgium

[11]Department of Physics, University of Warwick, Gibbet Hill Road, Coventry, CV4 7AL, UK

[12]Smithsonian Astrophysical Observatory, 60 Garden St., Cambridge, MA 02138, USA

[13]Department of Astronomy, The University of Tokyo, 7-3-1 Hongo, Bunkyo-ku, Tokyo, 113-0033, Japan

orbits that are nearly in a 3:2 mean-motion resonance. Here, we present results of ground-based follow-up observations for the K2-19 planetary system. We have performed high-dispersion spectroscopy and high-contrast adaptive-optics imaging of the host star with the HDS and HiCIAO on the Subaru 8.2m telescope. We find that the host star is relatively old ($\geq$ 8 Gyr) late G-type star ($T_{\rm eff} \sim 5350$ K, $M_{\rm s} \sim 0.9\ M_{\odot}$, and $R_{\rm s} \sim 0.9\ R_{\odot}$). We do not find any contaminating faint objects near the host star which could be responsible for (or dilute) the transit signals. We have also conducted transit follow-up photometry for the inner planet with KeplerCam on the FLWO 1.2m telescope, TRAPPISTCAM on the TRAPPIST 0.6m telescope, and MuSCAT on the OAO 1.88m telescope. We confirm the presence of transit-timing variations, as previously reported by Armstrong and coworkers. We model the observed transit-timing variations of the inner planet using the synodic chopping formulae given by Deck & Agol (2015). We find two statistically indistinguishable solutions for which the period ratios ($P_{\rm c}/P_{\rm b}$) are located slightly above and below the exact 3:2 commensurability. Despite the degeneracy, we derive the orbital period of the inner planet $P_{\rm b} \sim 7.921$ days and the mass of the outer planet $M_{\rm c} \sim 20 M_{\oplus}$. Additional transit photometry (especially for the outer planet) as well as precise radial-velocity measurements would be helpful to break the degeneracy and to determine the mass of the inner planet.

Subject headings: planets and satellites: individual (K2-19b, K2-19c) — stars: individual (K2-19) — techniques: high angular resolution — techniques: photometric — techniques: spectroscopic

1. Introduction

Kepler's two-wheel mission, K2, has been in operation since 2014 (Howell et al. 2014). K2 observes a number of campaign fields in the ecliptic plane for about 83 days each, and releases photometric data at intervals of about 3 months. Because many of the proposed target stars for K2 are somewhat brighter than the planet-hosting stars discovered by the original Kepler mission, the planets discovered by K2 are often good targets for further characterization. For this reason, planet searches based on K2 photometric data and subsequent follow-up observations are being conducted by many groups (Vanderburg & Johnson 2014; Montet et al. 2015; Foreman-Mackey et al. 2015; Crossfield et al. 2015; Sanchis-Ojeda et al. 2015).

EPIC201505350 (also designated K2-19) is one of the multi-transiting planetary sys-

tems discovered in campaign field 1 (Montet et al. 2015; Foreman-Mackey et al. 2015). An interesting feature of this system is that two transiting planets (K2-19b and K2-19c) have orbits that are close to a 3:2 mean-motion resonance (MMR). The formation of 3:2 MMR planet pairs through planetary migration has been the subject of extensive theoretical investigations (e.g., Papaloizou & Szuszkiewicz 2005; Raymond et al. 2008; Ogihara & Kobayashi 2013); however, the number of 3:2 MMR pairs actually discovered to date is still small. Thus K2-19 offers the prospect of a well-characterized example for theoretical studies of planet formation, as one can determine the mass, radius, and density of both planets, at least in principle.

The phenomenon of transit-timing variations (TTVs) can be used to estimate the mass of planets that are in or near resonances (Agol et al. 2005; Holman & Murray 2005). Recent theoretical studies have shown that the TTV of near-MMR planet pairs can be calculated analytically (Lithwick et al. 2012; Nesvorný & Vokrouhlický 2014; Deck & Agol 2015), facilitating the analysis. As both K2-19b and c are transiting, it may be possible to determine or constrain the mass of both planets through TTV monitoring. Ground-based transit follow-up observations for this system are very important, since the monitoring period of K2 was limited to about 83 days. Even though no TTV were detected during the interval of the K2 observations, recently Armstrong et al. (2015) reported on subsequent observations of K2-19b using the NITES 0.4m telescope and showed that the planet experienced a large TTV. They used a formula by Lithwick et al. (2012) to put an upper bound of $\sim$300 $M_\oplus$ on the masses of K2-19b and c. Further transit follow-up observations are needed to place a more stringent upper bound, or to determine the masses of the planets.

Another interesting feature of K2-19 is that the inner planet is a super-Neptune with the radius of about 7 $R_\oplus$ (or 0.7 $R_{\rm Jup}$). Based on an examination of the NASA Exoplanet Archive (Akeson et al. 2013), planets in that size range appear to be relatively infrequent among the sample of known transiting planets. Only a small number of super-Neptune-sized planets, such as HATS-7b (V=13.34, Bakos et al. 2015) and HATS-8b (V=14.03, Bayliss et al. 2015), have been discovered. Further, K2-19 is a unique MMR system in that the inner planet (super-Neptune-size) is about 1.7 times bigger than the outer planet (Neptune-size). This is not the case for the majority of 3:2 MMR planet pairs discovered by the Kepler (Ciardi et al. 2013), as discussed later in this paper. Those facts make it interesting to investigate the origin of K2-19 system as well as the internal and atmospheric compositions of both planets.

Another issue regarding this system is that the stellar parameters of the host star, such as the stellar mass and radius, have been characterized with only low signal-to-noise ratio (SNR of $\sim$ 25), moderately high spectral resolution ($R \sim 39,000$) spectra (see Armstrong et al. 2015). Thus there is room for improvement in the estimation of stellar parameters with

higher SNR and higher spectral resolution spectra. Furthermore, the possibility has not yet been excluded that there is a faint neighboring star with the photometric aperture of the K2 detector, which could be responsible for the transit signals or which could affect the observed amplitude of the signals. Both characterization of the host star with high dispersion spectroscopy and high-contrast direct imaging are important for a precise determination of the masses and radii of the planets.

Motivated by the preceding considerations, we have conducted three types of ground-based follow-up observations. The first one is high-dispersion spectroscopy to characterize the host star. The second one is high-contrast adaptive-optics (AO) imaging to check on any possible contamination from a faint companion star. The third one is ground-based time-series photometry of transits, to measure additional transit times and enhance the TTV analysis. The rest of this paper is organized as follows. We introduce our observations and reduction procedures in section 2. We describe our analysis methods and results in section 3. Based on the derived transit parameters, we further analyze the TTVs of the planets in section 4.1. We also discuss possible internal compositions and origins of the planets from a theoretical point of view in section 4.2 and 4.3. Finally, we summarize our study in section 5.

2. Observations and Reductions

2.1. Subaru 8.2m Telescope / HDS

In order to improve on estimates of the stellar parameters, we observed K2-19 with High Dispersion Spectrograph (HDS) on the Subaru 8.2m telescope on 2015 May 29 (UT). To maximize the SNR as well as to achieve a sufficient spectral resolution, we employed the Image Slicer #2 (Tajitsu et al. 2012, ; $R \sim 80,000$) and the standard I2a setup, simultaneously covering the spectral range between 4950-7550 Å with the two CCD chips. The raw spectrum was subjected to the standard IRAF[1] procedures to extract the one-dimensional (1D) spectrum. The wavelength scale was established by observations of the comparison Thorium-Argon lamp taken during evening and morning twilight. The exposure time was 20 minutes. The 1D spectrum has a SNR of ~ 70 per pixel in the vicinity of the sodium D lines.

[1]The Image Reduction and Analysis Facility (IRAF) is distributed by the National Optical Astronomy Observatory, which is operated by the Association of Universities for Research in Astronomy (AURA) under a cooperative agreement with the National Science Foundation.

2.2. Subaru 8.2m Telescope / HICIAO & AO188

We observed K2-19 in the H band with the HiCIAO (Tamura et al. 2006) combined with the AO188 (188 element curvature sensor adaptive optics system: Hayano et al. 2008), mounted on the 8.2m Subaru Telescape on 2015 May 8 (UT). We used the target star itself as a natural guide star for AO188, and employed an atmospheric dispersion corrector (ADC) to prevent the star from drifting on the detector due to differential refraction between the visible and near-infrared bands. The field of view (FOV) was $20'' \times 20''$, and the typical AO-corrected seeing was $\sim 0''.1$ on the night of our observations. The observations were conducted in the pupil tracking mode to enable the angular differential imaging (ADI; Marois et al. 2006) technique. We took 35 object frames with an exposure time of 30 s. The total exposure time was 17.5 min. As a first step in the reduction, we removed a characteristic stripe bias pattern from each image (Suzuki et al. 2010). Then, bad pixel and flat field correction were performed. Finally, the image distortions were corrected, using calibration images of the globular cluster M5 that were obtained on the same night.

2.3. FLWO 1.2m Telescope / KeplerCam

We observed one transit of K2-19 on 2015 January 28 (UT) with the 1.2m telescope at the Fred Lawrence Whipple Observatory (FLWO) on Mt. Hopkins, Arizona. We used Keplercam, which is equipped with a 4096×4096 pixel CCD with a $23'.1 \times 23'.1$ FOV. We observed through a Sloan i' filter. The exposure time was 30 s. Debiasing and flat-fielding (using dome flats) were performed using standard IRAF procedures. Aperture photometry was performed with custom routines written in the Interactive Data Language (IDL). We selected the final aperture size of 7 pixels in the 2×2 binning configuration, which means the radius of the aperture is about 5". The sky level per pixel was estimated from the median value in an annulus surrounding the aperture, with a radius that is about twice the aperture radius. The time of each exposure was recorded in UT, and the systematic error of the recorded time with respect to the standard clock was much smaller than the statistical uncertainty for the mid-transit time.

2.4. TRAPPIST 0.6m Telescope / TRAPPISTCAM

One transit of K2-19b was observed on the night of 2015 Feb 28 (UT) with the 0.6m TRAPPIST robotic telescope (TRAnsiting Planets and PlanetesImals Small Telescope), located at ESO La Silla Observatory (Chile). TRAPPIST is equipped with a thermoelectrically-

cooled 2K×2K CCD, which has a pixel scale of 0.″65 that translates into a $22' \times 22'$ FOV. For details of TRAPPIST, see Gillon et al. (2011) and Jehin et al. (2011). The transit was observed in an Astrodon Exoplanet (blue-blocking) filter that has a transmittance over 90% from 500 nm to beyond 1000 nm. The exposure time was 10 s. The time of each exposure was recorded in $\mathrm{HJD_{UTC}}$. During the run, the positions of the stars on the chip were maintained to within a few pixels thanks to a software guiding system that regularly derives an astrometric solution for the most recently acquired image and sends pointing corrections to the mount if needed. After a standard pre-reduction (bias, dark, and flat-field correction), the stellar fluxes were extracted from the images using the IRAF / DAOPHOT aperture photometry software (Stetson 1987). After testing several sets of reduction parameters, we chose the one giving the most precise photometry for the stars of similar brightness as the target. Differential photometry of the target star was performed relative to a selected set of reference stars. The set of reference stars was chosen as the one that gives the lowest root-mean-square (rms) transit light curve. It consists of nine stable stars of similar brightness and color to the target.

2.5. OAO 1.88m Telescope / MuSCAT

We observed one transit of K2-19b with a new multi-color camera, named MuSCAT, installed on the 1.88m telescope in Okayama Astrophysical Observatory (OAO) on 2015 April 25 (UT). On that night, a full transit was predicted to be observable based on the ephemeris of Foreman-Mackey et al. (2015). However, based on the updated ephemeris of Armstrong et al. (2015) (taking TTVs into account) only a partial transit was predicted to be observable. MuSCAT equips 3 CCD cameras and has a capability of 3-color simultaneous imaging in g'_2, r'_2, and $z_{s,2}$ bands of Astrodon Sloan Gen 2 filters (Narita et al. 2015; Fukui et al. 2015). Each CCD camera has a 6.′1×6.′1 FOV, with a pixel scale of about 0.″358. For the g'_2 and r'_2 band observations, we employed the high-speed readout mode (2 MHz, corresponding readout time of about 0.58 s and readout noise of $\sim$ 10 $\mathrm{e^-}$). For the $z_{s,2}$ band observations we used the low-speed readout mode (100 kHz, corresponding to readout time of about 10 s and readout noise of $\sim$ 4 $\mathrm{e^-}$) because at that time the $z_{s,2}$-band CCD was affected by excess readout noise (over 20 $\mathrm{e^-}$) in the high-speed readout mode[2]. The exposure times were 60 s, 30 s, and 60 s for g'_2, r'_2, and $z_{s,2}$ bands, respectively. Bias subtraction, flat-fielding, and aperture photometry are performed by a customized pipeline (Fukui et al. 2011). Aperture radii are selected as 17, 18, and 19 pixels for g'_2, r'_2, and $z_{s,2}$ bands, respectively. Sky level is measured in the annulus with the inner radius of 45 pixels

[2]The CCD has since been repaired and the readout noise problem has been fixed.

and the outer radius of 55 pixels. For differential photometry, we select a reference star UCAC4 453-052399 (g=12.53, r=12.11, i=11.96, J=11.08), which is slightly brighter than the target star (g=13.36, r=12.76, i=12.57, J=11.60). The aperture radii and the reference star were chosen so that rms of residuals for trial transit fittings are minimized.

2.6. NITES 0.4m telescope

For a more comprehensive transit analysis, we also analyze the previously published data from the NITES (Near Infra-red Transiting ExoplanetS: McCormac et al. 2014) 0.4m telescope in the same manner as our own data. The NITES data are identical with those presented by Armstrong et al. (2015). The transit observed by NITES was the same as the one observed by TRAPPIST.

3. Analyses and Results

3.1. Host Star Parameters from High Dispersion Spectroscopy

Using the high-resolution spectrum obtained with Subaru/HDS, we extract the atmospheric parameters (the effective temperature $T_{\rm eff}$, surface gravity $\log g$, metallicity [Fe/H], and microturbulent velocity ξ) by measuring the equivalent widths of iron I/II lines (Takeda et al. 2002), which are widely distributed throughout the observed wavelength region. We then translate those atmospheric parameters into estimates of the stellar mass and radius, using the Yonsei-Yale stellar-evolutionary models (Yi et al. 2001). Finally, the projected stellar rotation velocity $V \sin I_s$ is estimated by fitting the observed spectrum with the theoretically-generated intrinsic stellar absorption line profile, convolved with a kernel taking into account rotational and macroturbulent broadening (Gray 2005) and the instrumental profile (IP) of Subaru/HDS. The theoretical synthetic spectrum was taken from ATLAS9 model (a plane-parallel stellar atmosphere model in LTE: Kurucz 1993). The result of the spectroscopic analysis is summarized in Table 1. See Hirano et al. (2014) for details on how the uncertainties in these spectroscopic parameters are determined. The derived parameters are consistent with those reported by Armstrong et al. (2015), and have a higher precision by about an order of magnitude thanks to higher SNR spectra. We also find that the host star is likely older than $\sim$8 Gyr, which is far older than the typical planet formation and migration timescale ($\sim 10^7$ yr, see also Section 4.2).

3.2. Constraint on Contaminating Stars from AO Imaging

We employ the locally optimized combination of images (LOCI: Lafrenière et al. 2007) algorithm to maximize the efficiency of the ADI technique and to search for fainter objects in the inner region around K2-19. We estimate our achieved contrast ratio as follows. The final image of a LOCI pipeline is convolved with the PSF of the unsaturated image. The 1σ limit on the contrast ratio is defined as the ratio of the standard deviation of the pixel values inside an annulus of width 6 pixels to the stellar flux in the unsaturated image. Then the contrast ratio is corrected for a self-subtraction effect, which is estimated from the recovery rate of injected signals. Figure 1 shows a signal-to-noise ratio (SNR) map of a LOCI-reduced image around K2-19 (North is up and East is to the left). There are no other faint sources around K2-19 with SNR exceeding 5, except for a faint source located at the west-northwest edge of the image ($\sim$11.″5 from the center). The faint source has a contrast of $\sim 4 \times 10^{-4}$ relative to the brightness of K2-19 and locates outside the Kepler's PSF. Thus the presence of the faint source does not affect the light curves from K2 and other ground-based telescopes. We plot the 5σ contrast limit in Figure 2. Contrast limits of $\sim 2 \times 10^{-3}$ and $\sim 10^{-4}$ are achieved at distances of at 0.″4 and 1" from the host star, respectively. Thus we have not identified any contaminating faint object which can dilute or mimic the transits of K2-19b and K2-19c.

3.3. Reanalysis of K2 Light Curve

We analyze the light curve for K2-19 that has been produced from the raw pixel data by the ESPRINT collaboration. See Sanchis-Ojeda et al. (2015) for a description of the procedures for extracting the light curve from the K2 pixel data. We fit the K2 light curve by the procedure below and derive the best-fit system parameters along with mid-transit times. First, we separate the entire light curve into fourteen segments, each of which spans a transit. Three of the segments involve double transits (see Figure 3), during which two planets simultaneously transit the host star. We note that Armstrong et al. (2015) did not model those mutual transit events. Each segment includes the data within $\sim$ 4.5 hours of the predicted ingress/egress times (based on the ephemeris by Armstrong et al. 2015), which is sufficient to span the transit event as well as some time beforehand and afterward. For each segment, we compute the standard deviation of the out-of-transit fluxes, and adopt the standard deviation as an initial estimate of the uncertainty in each flux value.

All the light curve segments are fitted simultaneously with the common system parameters along with mid-transit time(s) for each segment. We compute the posterior distributions for those parameters based on the Markov Chain Monte Carlo (MCMC) algorithm, assuming

that the likelihood is proportional to $\exp(-\chi^2/2)$ where

$$\chi^2 = \sum_i \frac{(f^{(i)}_{\rm LC,obs} - f^{(i)}_{\rm LC,model})^2}{\sigma^{(i)2}_{\rm LC}}, \quad (1)$$

where $f^{(i)}_{\rm LC,obs}$ and $\sigma^{(i)}_{\rm LC}$ are the i-th observed K2 flux and its error, respectively. We employ the transit model by Ohta et al. (2009) integrated over the 29.4-minute averaging time of the *Kepler* data. We neglect the impact of any possible planet-planet eclipses (Hirano et al. 2012) on the light curve shape, due to the rather sparse sampling of the K2 data. Finally, to obtain the model flux $f^{(i)}_{\rm LC,model}$, the integrated light curve model for each segment is multiplied by a second-order polynomial function of time, representing the longer-timescale flux variations at the time of the transit. Therefore, the adjustable parameters in our model are (for each planet) the scaled semi-major axis a/R_s, the transit impact parameter b, and the planet-to-star radius ratio R_p/R_s; the quadratic limb-darkening parameters u_1 and u_2; the mid-transit time(s) T_c for each segment; and the coefficients of the second-order polynomials. Because the sparse sampling of the K2 data relative to the timescale of ingress and egress prohibits us from constraining the orbital eccentricity e of either planet based only on the transit light curve (Dawson & Johnson 2012), we simply assume $e = 0$ for both planets.

Following the procedure described in Hirano et al. (2015), we compute the posterior distributions for the parameters listed above; we first optimize Equation (1) using Powell's conjugate direction method, allowing all the relevant parameters to vary. At this point, we compute the level of time-correlated noise β (so-called red noise: Pont et al. 2006; Winn et al. 2008) for each segment, and inflate the errors in each segment by β. We then fix the coefficients of the polynomial functions to the optimized values and perform the MCMC computation starting from the initial best-fit values for the other parameters. The step size for each parameter is iteratively optimized such that the final acceptance ratio over the whole chain is between 15–35%. We extend the chains to 10^7 links, given the relatively large number of free parameters. We employ the median, and 15.87 and 84.13 percentiles of the marginalized posterior distribution of each parameter to convey the representative value and its $\pm1\sigma$ errors. As a check on convergence, we repeat the analysis after changing the initial input values for the system parameters, and find no dependence on the initial values. We report the values and uncertainties of the basic transit parameters in Table 2, and we report the mid-transit times as well as the β factor for each segment in Table 3. Combining the $R_{\rm p}/R_{\rm s}$ values with the $R_{\rm s}$ value listed in Table 1, we estimate the planetary radii of K2-19b and K2-19c as $R_{\rm p,b} = 7.34 \pm 0.27 R_\oplus$ and $R_{\rm p,c} = 4.37 \pm 0.22 R_\oplus$, respectively. The planetary radii are also presented in Table 2.

3.4. Modeling of New Transit Light Curves

Our procedure for modeling the ground-based transit light curves follows Narita et al. (2013). First, the time stamps of the photometric data are placed onto the $\mathrm{BJD_{TDB}}$ system using the code by Eastman et al. (2010). We check all the light curves by eye and eliminate obvious outliers. We then fit the transit light curves simultaneously, using an analytic transit light curve model and various choices to describe the more gradual out-of-transit (baseline) flux variations.

We adopt baseline model functions $F_{\rm oot}$ described as follows,

$$\begin{aligned} F_{\rm oot} &= k_0 \times 10^{-0.4\Delta m_{\rm cor}}, \\ \Delta m_{\rm cor} &= \sum k_i X_i, \end{aligned}$$

where k_0 is the normalization factor, $\{\mathbf{X}\}$ are observed variables, and $\{\mathbf{k}\}$ are the coefficients (Fukui et al. 2013). In order to select the most appropriate baseline models for the light curves, we adopt the Bayesian Information Criteria (BIC: Schwarz 1978). The BIC value is given by $\mathrm{BIC} \equiv \chi^2 + k \ln N$, where k is the number of free parameters, and N is the number of data points. For the variables $\{\mathbf{X}\}$, we test various combinations of time (t), airmass (z), the relative centroid positions in x (dx) and y (dy), and the sky background counts (s). In addition, we also allowed an additional factor $k_{\rm flip}$ to account for a change of the normalization factor after the meridian flip for the TRAPPIST light curve. Based on minimum BIC, we adopt k_0. t and z to be fitting parameters for FLWO and MuSCAT; k_0, z, and $k_{\rm flip}$ for TRAPPIST; and k_0 and t for NITES, respectively.

For the transit light curve model, we employ a customized code (Narita et al. 2007) that use the analytic formula by Ohta et al. (2009). The formula is equivalent to that of Mandel & Agol (2002) when using the quadratic limb-darkening law, $I(\mu) = 1 - u_1(1-\mu) - u_2(1-\mu)^2$, where I is the intensity and μ is the cosine of the angle between the line of sight and the line from the position of the stellar surface to the stellar center. We refer the tables of quadratic limb-darkening parameters by Claret et al. (2013), and compute allowed $u_1 + u_2$ and $u_1 - u_2$ values for $T_{\rm eff} = 5300$ K or 5400 K and $\log g = 4.0$ or 4.5, based on the stellar parameters presented in Table 1. We adopt uniform priors for $u_1 + u_2$ and $u_1 - u_2$ as follows: [0.59, 0.61] and [0.24, 0.34] for FLWO i', [0.77, 0.85] and [0.67, 0.82] for MuSCAT g'_2, [0.68, 0.70] and [0.35, 0.46] for MuSCAT r'_2, [0.52, 0.55] and [0.17, 0.26] for MuSCAT $z_{s,2}$, and [0.67, 0.70] and [0.38, 0.50] for TRAPPIST and NITES. We assume an orbital period $P = 7.921$ days and a reference epoch for the transits $T_{\rm c,0} = 2457082.6895$, the values reported by Armstrong et al. (2015) based on the NITES data. We note that these assumptions have little impact on the resultant transit parameters, because we allow $T_{\rm c}$ to be a free parameter, and the uncertainty in P is negligible. To constrain the mid-transit times

precisely even without complete coverage of the entire transit event, we place an *a priori* constraint on the total transit duration, $T_{14} = 0.1365 \pm 0.0017$, based on our K2 analysis. We allow $R_{\rm p}/R_{\rm s}$, $a/R_{\rm s}$, and the orbital inclination i to be free parameters.

First we optimize free parameters for each light curve, using the AMOEBA algorithm (Press et al. 1992). The penalty function is also given by Eq. (1), where $f^{(i)}_{\rm LC,model}$ is a combination of the baseline model and the analytic transit formula mentioned above. Then if the reduced χ^2 is larger than unity, we rescale the photometric errors of the data such that the reduced χ^2 for each light curve becomes unity. We also estimate the level of time-correlated noise for each light curve, and further rescale the errors by multiplying β factors listed in Table 4. Finally, we use the MCMC method (Narita et al. 2013) to evaluate values and uncertainties of the free parameters. For the FLWO, TRAPPIST, and NITES light curves, we fit each light curve independently. We create 5 chains of 10^6 points for each light curve, and discard the first 10^5 points from each chain (the "burn-in" phase). The jump sizes are adjusted such that the acceptance ratios are 20–30%. For the OAO/MuSCAT light curves, we fit the 3-band data simultaneously, requiring consistency in the parameters $T_{\rm c}$, i, and $a/R_{\rm s}$. We create 5 chains of 3×10^6 points for MuSCAT light curves, and discard the first 3×10^5 points from each chain. The acceptance ratios are set to about 25%. Table 4 lists the median values and $\pm1\sigma$ uncertainties, which are defined by the 15.87 and 84.13 percentile levels of the merged posterior distributions. The baseline corrected transit light curves are plotted in Figure 4 (FLWO), Figure 5 (TRAPPIST and NITES), and Figure 6 (OAO).

4. Discussion

4.1. Transit Timing Variations and the Mass of the Outer Planet

Since K2-19b and K2-19c are close to the 3:2 MMR, it is not surprising that large TTVs have been observed in this system. To explain the observed mid-transit times, we adopt the analytic formulae of TTV by Deck & Agol (2015) and Nesvorný & Vokrouhlický (2014), who considered the synodic chopping effect. Successful modeling of the synodic chopping effect enables us to estimate the mass of a perturbing body. In particular the resulting mass determination is not subject to the mass-eccentricity degeneracy that was discussed by Lithwick et al. (2012), who derived analytic formulae for a pair of planets near a first-order MMR. Although the chopping analytic formulae are only applicable to systems with nearly circular and coplanar orbits, those requirements are likely fulfilled in this case, given the presence of mutual transits and the requirement for long-term dynamical stability.

The chopping formulae predict the TTVs of the inner and outer planets as follows:

$$\delta t_b = \sum_{j=1}^{\infty} \frac{P_b}{2\pi} \mu_c f_b^{(j)}(\alpha) \sin\psi_j, \quad (2)$$

$$\delta t_c = \sum_{j=1}^{\infty} \frac{P_c}{2\pi} \mu_b f_c^{(j)}(\alpha) \sin\psi_j, \quad (3)$$

where $\mu_{b,c}$ are the planet-to-star mass ratio ($M_{b,c}/M_s$) respectively, and

$$f_b^{(j)}(\alpha) = -\alpha \frac{j(\beta^2+3)b_{1/2}^j(\alpha) + 2\alpha\beta\frac{\partial}{\partial\alpha}b_{1/2}^j(\alpha) - \alpha\delta_{j,1}(\beta^2+2\beta+3)}{\beta^2(\beta^2-1)}, \quad (4)$$

$$f_c^{(j)}(\alpha) = \frac{j(\kappa^2+3)b_{1/2}^j(\alpha) + 2\kappa(\alpha\frac{\partial}{\partial\alpha}b_{1/2}^j(\alpha) + b_{1/2}^j(\alpha)) - \alpha^{-2}\delta_{j,1}(\kappa^2-2\kappa+3)}{\kappa^2(\kappa^2-1)}, \quad (5)$$

$$b_{1/2}^j(\alpha) = \frac{1}{\pi}\int_0^{2\pi} \frac{\cos(j\theta)}{\sqrt{1-2\alpha\cos\theta+\alpha^2}} d\theta. \quad (6)$$

Note that $P_{b,c}$ and $\mu_{b,c}$ are defined as non-negative variables. The parameters α, β, and κ are defined as, $\alpha = a_b/a_c$, $\beta = j(n_b - n_c)/n_b$, and $\kappa = j(n_b - n_c)/n_c$, where $a_{b,c}$ and $n_{b,c}$ are the semi-major axes and the mean motions of the planets. Those parameters can be expressed by the periods of the planets: $\alpha \simeq (P_b/P_c)^{2/3}$ (using Kepler's third law and neglecting the planet masses in comparison to the stellar mass), $\beta = j(1 - P_b/P_c)$, and $\kappa = j(P_c/P_b - 1)$. Note that $\delta_{j,1}$ represents Kronecker's delta, which is 1 when $j = 1$ and 0 for $j > 1$. When the time of conjunction ($t_{\rm conj}$) is used as the origin of the time scale, the phase ψ_j can be expressed simply as

$$\psi_j = 2\pi t j(1/P_b - 1/P_c) \equiv 2\pi t j/P_{\rm syn}, \quad (7)$$

where $P_{\rm syn}$ is the synodic period. For the current system, we derive $t_{\rm conj} = 2456852.9344 \pm 0.0022\,{\rm BJD_{TDB}}$ from one of the mutual transit events, assuming that both planets are orbiting in the same direction. Consequently, the observed mid-transit times (T_c) for the planets can be modeled by 6 free parameters $T_c(0)_{b,c}$, $P_{b,c}$, and $\mu_{b,c}$ as:

$$T_c(E_b)_b = T_c(0)_b + P_b \times E_b + \delta t_b, \quad (8)$$

$$T_c(E_c)_c = T_c(0)_c + P_c \times E_c + \delta t_c, \quad (9)$$

where $E_{b,c}$ are the transit epochs of the planets with the origins at the first K2 transits.

We first try to find an optimal parameter set for the 6 parameters ($T_c(0)_b$, $T_c(0)_c$, P_b, P_c, μ_b and μ_c) by minimizing

$$\chi^2 = \sum_i \frac{(T_{\rm c,obs}^{(i)} - T_{\rm c,model}^{(i)})^2}{\sigma_{T_{\rm c}}^{(i)2}}, \quad (10)$$

using the AMOEBA algorithm. In evaluating Equations (2) and (3), we truncate the series at $j = 7$ to reduce the computational cost. We model the observed the mid-transit times for both planets listed in Table 3 and 4 (21 in total) using the equations above. However, we find that the AMOEBA algorithm does not converge. Note that we have tested the effects of including higher orders of j in the calculation, but the result remains unchanged. Apparently there are multiple local minima of χ^2 in the parameter space, which are almost equally favored. This result is quite understandable: we have not observed any additional transits of planet c since the end of the K2 campaign, and hence the TTVs of planet c are poorly constrained.

For this reason, we decide to fit only the mid-transit times of the inner planet (14 in total) using the corresponding 4 parameters ($T_c(0)_b$, P_b, P_c, and μ_c). This time the AMOEBA algorithm converges. Table 5 summarizes the optimal parameters and Figure 7 plots the optimal model explaining the observed TTVs of the inner planet. We note that we find a somewhat large reduced χ^2, namely $\chi^2/\nu \sim 4.4$, where $\nu = 10$ is the number of degrees of freedom. This may indicate that the uncertainties in T_c, particularly those based on K2 data, have been underestimated by a factor of about 2.1. To account for possible systematic errors, the uncertainties given in Table 5 have been enlarged by a factor of $\sqrt{\chi^2/\nu}$ from the original 1σ errors estimated by the usual criterion $\Delta\chi^2 = 1.0$.

We then check on the existence of possible local minima of χ^2 by fixing P_c close to the optimal value and optimizing the other parameters using the AMOEBA algorithm. We repeat this exercise for values of P_c ranging from 11.5 to 12.5. Figure 8 shows the variation in χ^2 and the optimal parameters with changing P_c. We find that the second-minimum χ^2 is located at $P_c \sim 11.775$ days with $\Delta\chi^2 = 5.4$ from the minimum χ^2. Figure 9 presents a TTV model for the second-minimum χ^2. The behavior of the second-minimum χ^2 model is almost identical to the minimum χ^2 model in the observing period. Thus we cannot exclude this solution statistically at this point. Therefore, Table 5 also gives the parameters and errors based on the second-minimum χ^2 solution. We also note that the third-minimum χ^2 is located at $P_c \sim 12.17$ days with $\chi^2 \sim 67.50$, which is statistically less favorable than the above two solutions.

As seen in Figure 8, the orbital period for the inner planet P_b is robustly determined to be about 7.921 days. The minimum and second-minimum χ^2 are thus located slightly above ($P_c/P_b = 1.51531 \pm 0.00117$) and below ($P_c/P_b = 1.48651 \pm 0.00180$) the exact 3:2 commensurability ($P_c \sim 11.882$ days). The orbital period of the outer planet is not permitted to lie exactly on the commensurability, where larger TTVs are predicted and the synodic chopping formulae are less reliable. This is why the optimization results in the mass of the planet c being driven to zero when P_c is held fixed near the 3:2 commensurability. The

planet-to-star mass ratio for the outer planet μ_c is estimated as 0.0000713 ± 0.0000027 for the minimum χ^2 solution and 0.0000672 ± 0.0000039 for the second-minimum. According to the mass of the host star presented in Table 1, these values correspond to a mass for planet c of $21.4 \pm 1.9 M_\oplus$ and $20.2 \pm 2.7 M_\oplus$ for the minimum and second-minimum solutions, respectively. Thus the mass of the outer planet is well constrained to be $\sim 20 M_\oplus$. We note that the error of $t_{\rm conj}$ has less impact on the above results. Finally, we present coefficients of the synodic chopping formulae in Table 5 so as to facilitate transit predictions for the inner planet in upcoming years.

Very recently, Barros et al. (2015) reported a photo-dynamical modeling of TTVs and RVs of the K2-19 system. They derived the mass of the planet c as $15.9^{+7.9}_{-2.8} M_\oplus$, which is well consistent with our result. We note that the derived orbital periods of both planets are also consistent when taking account for a difference in the definitions[3] of $P_{\rm b}$ and $P_{\rm c}$.

4.2. Internal compositions of K2-19b and 19c

K2-19c has a relatively low mean density of $1.43\,{\rm g\,cm^{-3}}$. It is therefore likely to have a gaseous atmosphere on top of any solid component (see also Figure 10). We explore models for the interior structure of K2-19c ($21.4\,M_\oplus$, $4.37\,R_\oplus$ at $0.1024\,{\rm AU}$) based on the condition of hydrostatic equilibrium, using equations of state (EoS) for four constituents: SCvH EoS for H/He (Saumon et al. 1995); the *ab initio* EoS (French et al. 2009) and the SESAME EoS 7150 (Lyon & Johnson 1992) for water; and the SESAME EoS 7100 and 2140 for rocky material and iron, respectively. We calculate a pressure-temperature profile of an irradiated planet's atmosphere in radiative equilibrium, using the analytical formulae of Parmentier & Guillot (2014) and gas opacities derived by Freedman et al. (2008). We assume that both the incoming and outgoing radiation fields are isotropic, the bond albedo of the planet is zero, and the incoming flux is averaged over the dayside hemisphere. The atmospheric mass fraction of K2-19c is estimated to be $\sim 7\%$ for a Earth-like core model (32.5% iron core, 67.5% silicate mantle) and $\sim 1.3\%$ for an icy core model (ice : rock = 2.7 : 1), where we assumed that K2-19c has a H/He atmosphere with the stellar metallicity of [Fe/H] = 0.07. We find that K2-19c likely has a H/He atmosphere of $\lesssim 10\,{\rm wt\%}$ despite the fact that its total mass exceeds the critical core mass for gas accretion within the protoplanetary disk, which is thought to be $\sim 10\,M_\oplus$ (e.g. Pollack et al. 1996). This suggests that

[3]We define $P_{\rm b}$ and $P_{\rm c}$ as linear coefficients for the epoch and they are decoupled from the TTV term (see equations 8 and 9), whereas Barros et al. (2015) defined them as parameters in the photo-dynamical modeling, which includes the TTV term (see Barros et al. 2015).

the atmospheric removal of K2-19c via giant impacts and/or a mass loss driven by stellar irradiation might have occurred.

The mass of K2-19b remains undetermined. Here, we discuss the possible mass range of K2-19b ($7.34\,R_\oplus$ at 0.0823 AU) from a standpoint of the formation and evolution of close-in planets. Under the extreme assumption that K2-19b has no gaseous atmosphere and is purely solid, its observed radius would require its mass to be $> 100\,M_\oplus$. The formation of such a massive solid core without any gaseous envelope seems unlikely. Such a massive core would be theoretically expected to initiate the (*in-situ*) accretion of the ambient disk gas (e.g. Ikoma & Hori 2012). A core of this mass has been inferred for HD 149026b (Sato et al. 2005), but in that case the core is accompanied by a substantial gaseous atmosphere. Consequently, for K2-19b, it seems most plausible to consider models that possess an atmosphere. However, we note that K2-19b, orbiting at only ~ 0.08 AU, may have undergone atmospheric loss due to stellar irradiation. As the age of K2-19 is relatively old (≥ 8 Gyr), a Neptune-mass planet could have lost a substantial amount of its atmosphere, whereas a Jupiter-mass planet would likely have retained its original atmosphere (e.g. Owen & Wu 2013).

With these considerations in mind, we consider two models that K2-19b is a Neptune-like planet ($\lesssim 20$ wt% of a H/He atmosphere) or a gas giant. We first suppose that K2-19b has a H/He atmosphere of 1 wt%, 10 wt%, and 20 wt% on top of a solid core. The atmosphere is taken to have the same metallicity as the host star, and the core is taken to have an Earth-like composition. Under these assumptions, the mass of K2-19b is expected to be $\sim 5.1\,M_\oplus$, $18\,M_\oplus$, and $37\,M_\oplus$, respectively. Second, we suppose that K2-19b has a mass of $1\,M_{\rm Jup}$. In this case the models indicate that the atmospheric mass fraction is $\sim 35\%$. Accordingly, K2-19b can be a sub-Neptune-mass planet with a tenuous atmosphere, a super-Neptune planet, or a close-in gas giant with an extremely massive solid core. Recently, Barros et al. (2015) derived the mass of K2-19b as 44 ± 12 $M_\oplus$, from photo-dynamical modeling. Their result supports that K2-19b would be surrounded by a thick H/He atmosphere of ~ 20 wt%.

4.3. A close-in super-Neptune and Neptune pair close to the 3:2 MMR

The K2-19 system is the first discovery of close-in Neptune-sized planets near a 3:2 MMR. A slow convergent migration allows low-mass planets to be locked into a first-order commensurability (e.g. Papaloizou & Szuszkiewicz 2005). In fact, Figure 11 shows that all of the other pairs of planets close to the 3:2 commensurability found by Kepler are smaller than $3\,R_\oplus$. Also, planets with $P \lesssim 10$ days near a 2:1 MMR have radii smaller than about $3\,R_\oplus$. The peculiar pair close to the 3:2 MMR around K2-19 is suggestive of inward transport of Neptune-sized planets through a convergent migration. We find there is a lack of close-in

gas giants among both 3:2 MMR and 2:1 MMR systems[4]. Besides, 3:2 MMR systems seem to be less common than 2:1 MMR ones. Dynamical instability of more closely-packed 3:2 MMR systems may be responsible for the feature. In addition, there is no gas giant in a 3:2 MMR so far discovered within $P = 50$ days. For 2:1 MMR systems, gas giants such as Kepler-9b, 9c (Holman et al. 2010), and Kepler-30c (Fabrycky et al. 2012) form the 2:1 commensurability beyond $P \sim 10$ days. The distinct habitat may imply that large planets with radius of $\gtrsim 3\,R_\oplus$ most likely fall into a 2:1 MMR rather than a 3:2 MMR due to the strength of planetary migration.

An outer planet formed in a 2:1 MMR or 3:2 MMR tends to be larger than an inner one (see Figure 11). This may imply that an outer planet caught up with an inner one to form a first-order MMR system in a protoplanetary disk. The inner planet closer to the central star loses its atmosphere more readily via stellar X-ray and UV (XUV) irradiation. The strength of the stellar XUV flux that a pair of planets in a $p : p + 1$ MMR receives is related as $\frac{F^{\rm out}}{F^{\rm in}} \propto \left(\frac{p}{p+1}\right)^{4/3}$, where p is the commensurability integer and F is the stellar XUV flux. The subtle but non-negligible flux difference may lead to the prevalence of larger outer planets in a 2:1 MMR or a 3:2 MMR. However, the radius of K2-19b is about 1.68 times as large as that of the Neptune-sized K2-19c. This means that the K2-19 system has a unique 3:2 MMR configuration, compared to other close-in MMR systems with smaller planets. The mass determination of K2-19b should be a crucial role of understanding what causes their radius contrast, and why the close-in super-Neptune and Neptune pair was trapped into a 3:2 MMR rather than a 2:1 MMR, for example, the difference in migration speed (Ogihara & Kobayashi 2013).

5. Summary

We have conducted high-dispersion spectroscopy, AO imaging, and ground-based transit follow-up observations to characterize the K2-19 planetary system. We have estimated parameters of the host star with an order of magnitude higher precision than previous studies by the Subaru/HDS spectroscopy. Through the Subaru/HiCIAO imaging, we have excluded the presence of contaminating faint objects which can dilute or mimic transits of the two planets. We have obtained new ground-based transit light curves using the FLWO 1.2m telescope, TRAPPIST 0.6m telescope, and OAO 1.88m telescope. Combined with the K2 transit light curves, we have modeled observed TTV for the inner planet using the synodic

[4]RV surveys have unveiled long-period gas giants in a 3:2 MMR (HD 45364 and HD 204313) and those in a 2:1 MMR (24 Sex, HD 128311, HD 37124, HD 155358, HD 73526, and HD 82943).

chopping formulae given by Deck & Agol (2015). We have found two statistically indistinguishable solutions for TTV, located slightly above and below the exact 3:2 MMR. Despite the degeneracy, both solutions consistently estimate the orbital period of the inner planet $P_{\rm b} \sim 7.921$ days and the mass of the outer planet $M_{\rm c} \sim 20 M_{\oplus}$.

To break the degeneracy of the TTV solutions, further ground-based transit follow-up observations as well as precise radial-velocity measurements are strongly desired. We particularly emphasize the importance of transit observations for the outer planet, which will allow us to characterize the TTV of the outer planet in detail and thereby enable us to estimate the mass of the inner planet precisely. Given the nearly-equatorial location of K2-19 in the sky (RA: 11:39:50.477, Dec: +00:36:12.87, Zacharias et al. 2013), the K2-19 system is observable from both the northern and southern hemispheres. This will facilitate intensive follow-up observations, which would be quite fruitful in the upcoming seasons. A precise estimate of the mass of the inner planet will allow us to estimate the amount of a H/He atmosphere, for which we have presented theoretical predictions based on different internal compositions. The nature and the amount of the H/He atmosphere for the inner planet can be further characterized by transmission spectroscopy. Since the inner planet is a rare case of a super-Neptune, such a characterization of the atmosphere would be also interesting as future work.

N.N. acknowledges supports by the NAOJ Fellowship, Inoue Science Research Award, and Grant-in-Aid for Scientific Research (A) (JSPS KAKENHI Grant Number 25247026). T.H. is supported by Japan Society for Promotion of Science (JSPS) Fellowship for Research (No. 25-3183). A.F. acknowledges supports by the Astrobiology Center Project of National Institutes of Natural Sciences (NINS) (Grant Number AB271009). Y.H. is supported by Grant-in-Aid for Scientific Research on Innovative Areas (No. 26103711) from MEXT. This work was performed, in part, under contract with the Jet Propulsion Laboratory (JPL) funded by NASA through the Sagan Fellowship Program executed by the NASA Exoplanet Science Institute. Work by J.N.W. was supported by the NASA Origins program (grant NNX11AG85G). M.G. and E.J. are Research Associates at the Belgian Fund for Scientific Research (Fonds National de la Recherche Scientifique, F.R.S-FNRS). L.D. received the support of the F.R.I.A. fund of the FNRS. TRAPPIST is a project funded by the F.R.S-FNRS under grant FRFC 2.5.594.09.F, with the participation of the Swiss National Science Foundation (SNF). M.T. is supported by Grant-in-Aid for Scientific Research (No.15H02063). This research has made use of the Exoplanet Orbit Database and the Exoplanet Data Explorer at exoplanets.org. We also thank Masahiro Ogihara for helpful comments on the dynamics of MMR systems.

Facilities: Subaru, OAO, FLWO, TRAPPIST, NITES.

REFERENCES

Agol, E., Steffen, J., Sari, R., & Clarkson, W. 2005, MNRAS, 359, 567

Akeson, R. L., et al. 2013, PASP, 125, 989

Armstrong, D. J., et al. 2015, A&A, 582, A33

Bakos, G. Á., et al. 2015, ArXiv e-prints arXiv:1507.01024

Barros, S. C. C., et al. 2015, ArXiv e-prints arXiv:1510.01047

Bayliss, D., et al. 2015, AJ, 150, 49

Ciardi, D. R., Fabrycky, D. C., Ford, E. B., Gautier, III, T. N., Howell, S. B., Lissauer, J. J., Ragozzine, D., & Rowe, J. F. 2013, ApJ, 763, 41

Claret, A., Hauschildt, P. H., & Witte, S. 2013, A&A, 552, A16

Crossfield, I. J. M., et al. 2015, ApJ, 804, 10

Dawson, R. I., & Johnson, J. A. 2012, ApJ, 756, 122

Deck, K. M., & Agol, E. 2015, ApJ, 802, 116

Eastman, J., Siverd, R., & Gaudi, B. S. 2010, PASP, 122, 935

Fabrycky, D. C., et al. 2012, ApJ, 750, 114

Foreman-Mackey, D., Montet, B. T., Hogg, D. W., Morton, T. D., Wang, D., & Schölkopf, B. 2015, ApJ, 806, 215

Freedman, R. S., Marley, M. S., & Lodders, K. 2008, ApJS, 174, 504

French, M., Mattsson, T. R., Nettelmann, N., & Redmer, R. 2009, Phys. Rev. B, 79, 054107

Fukui, A., et al. 2011, PASJ, 63, 287

Fukui, A., et al. 2013, ApJ, 770, 95

Fukui, A., et al. 2015, ArXiv e-prints arXiv:1510.03997

Gillon, M., Jehin, E., Magain, P., Chantry, V., Hutsemékers, D., Manfroid, J., Queloz, D., & Udry, S. 2011, in European Physical Journal Web of Conferences, Vol. 11, European Physical Journal Web of Conferences, 6002

Gray, D. F. 2005, The Observation and Analysis of Stellar Photospheres (UK: Cambridge University Press, 2005)

Han, E., Wang, S. X., Wright, J. T., Feng, Y. K., Zhao, M., Fakhouri, O., Brown, J. I., & Hancock, C. 2014, PASP, 126, 827

Hayano, Y., et al. 2008, in Presented at the Society of Photo-Optical Instrumentation Engineers (SPIE) Conference, Vol. 7015, Society of Photo-Optical Instrumentation Engineers (SPIE) Conference Series

Hirano, T., Masuda, K., Sato, B., Benomar, O., Takeda, Y., Omiya, M., Harakawa, H., & Kobayashi, A. 2015, ApJ, 799, 9

Hirano, T., Sanchis-Ojeda, R., Takeda, Y., Winn, J. N., Narita, N., & Takahashi, Y. H. 2014, ApJ, 783, 9

Hirano, T., et al. 2012, ApJ, 759, L36

Holman, M. J., & Murray, N. W. 2005, Science, 307, 1288

Holman, M. J., et al. 2010, Science, 330, 51

Howell, S. B., et al. 2014, PASP, 126, 398

Ikoma, M., & Hori, Y. 2012, ApJ, 753, 66

Jehin, E., et al. 2011, The Messenger, 145, 2

Kurucz, R. 1993, ATLAS9 Stellar Atmosphere Programs and 2 km/s grid. Kurucz CD-ROM No. 13. Cambridge, Mass.: Smithsonian Astrophysical Observatory, 1993., 13

Lafrenière, D., Marois, C., Doyon, R., Nadeau, D., & Artigau, É. 2007, ApJ, 660, 770

Lithwick, Y., Xie, J., & Wu, Y. 2012, ApJ, 761, 122

Lyon, S. P., & Johnson, J. D. 1992, LA-UR-92-3407, 1

Mandel, K., & Agol, E. 2002, ApJ, 580, L171

Marois, C., Lafrenière, D., Doyon, R., Macintosh, B., & Nadeau, D. 2006, ApJ, 641, 556

McCormac, J., Skillen, I., Pollacco, D., Faedi, F., Ramsay, G., Dhillon, V. S., Todd, I., & Gonzalez, A. 2014, MNRAS, 438, 3383

Montet, B. T., et al. 2015, ApJ, 809, 25

Narita, N., et al. 2007, PASJ, 59, 763

Narita, N., et al. 2013, ApJ, 773, 144

Narita, N., et al. 2015, Journal of Astronomical Telescopes, Instruments, and Systems, 1, 045001

Nesvorný, D., & Vokrouhlický, D. 2014, ApJ, 790, 58

Ogihara, M., & Kobayashi, H. 2013, ApJ, 775, 34

Ohta, Y., Taruya, A., & Suto, Y. 2009, ApJ, 690, 1

Owen, J. E., & Wu, Y. 2013, ApJ, 775, 105

Papaloizou, J. C. B., & Szuszkiewicz, E. 2005, MNRAS, 363, 153

Parmentier, V., & Guillot, T. 2014, A&A, 562, A133

Pollack, J. B., Hubickyj, O., Bodenheimer, P., Lissauer, J. J., Podolak, M., & Greenzweig, Y. 1996, Icarus, 124, 62

Pont, F., Zucker, S., & Queloz, D. 2006, MNRAS, 373, 231

Press, W. H., Teukolsky, S. A., Vetterling, W. T., & Flannery, B. P. 1992, Numerical recipes in C. The art of scientific computing (Cambridge: University Press, —c1992, 2nd ed.)

Raymond, S. N., Barnes, R., Armitage, P. J., & Gorelick, N. 2008, ApJ, 687, L107

Sanchis-Ojeda, R., et al. 2015, ArXiv e-prints arXiv:1504.04379

Sato, B., et al. 2005, ApJ, 633, 465

Saumon, D., Chabrier, G., & van Horn, H. M. 1995, ApJS, 99, 713

Stetson, P. B. 1987, PASP, 99, 191

Suzuki, R., et al. 2010, in Society of Photo-Optical Instrumentation Engineers (SPIE) Conference Series, Vol. 7735, Society of Photo-Optical Instrumentation Engineers (SPIE) Conference Series, 30

Tajitsu, A., Aoki, W., & Yamamuro, T. 2012, PASJ, 64, 77

Takeda, Y., Ohkubo, M., & Sadakane, K. 2002, PASJ, 54, 451

Tamura, M., et al. 2006, in Presented at the Society of Photo-Optical Instrumentation Engineers (SPIE) Conference, Vol. 6269, Ground-based and Airborne Instrumentation for Astronomy. Edited by McLean, Ian S.; Iye, Masanori. Proceedings of the SPIE, Volume 6269, pp. 62690V (2006).

Vanderburg, A., & Johnson, J. A. 2014, PASP, 126, 948

Winn, J. N., et al. 2008, ApJ, 683, 1076

Yi, S., Demarque, P., Kim, Y.-C., Lee, Y.-W., Ree, C. H., Lejeune, T., & Barnes, S. 2001, ApJS, 136, 417

Zacharias, N., Finch, C. T., Girard, T. M., Henden, A., Bartlett, J. L., Monet, D. G., & Zacharias, M. I. 2013, AJ, 145, 44

Zeng, L., & Sasselov, D. 2013, PASP, 125, 227

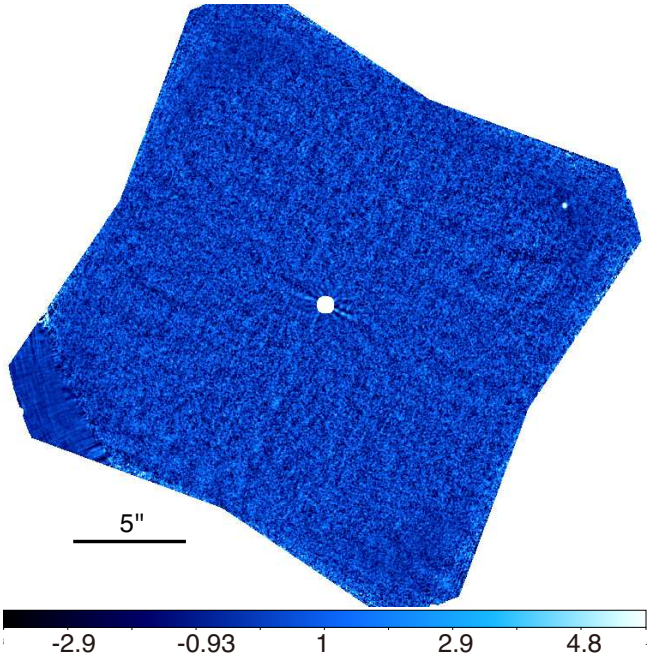

Fig. 1.— A signal-to-noise ratio (SNR) map around K2-19 processed by the LOCI algorithm. North is up and East

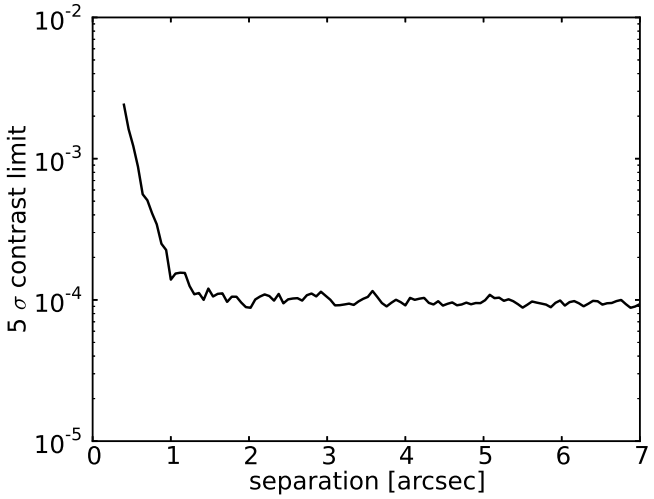

Fig. 2.— A 5σ contrast limit curve around K2-19.

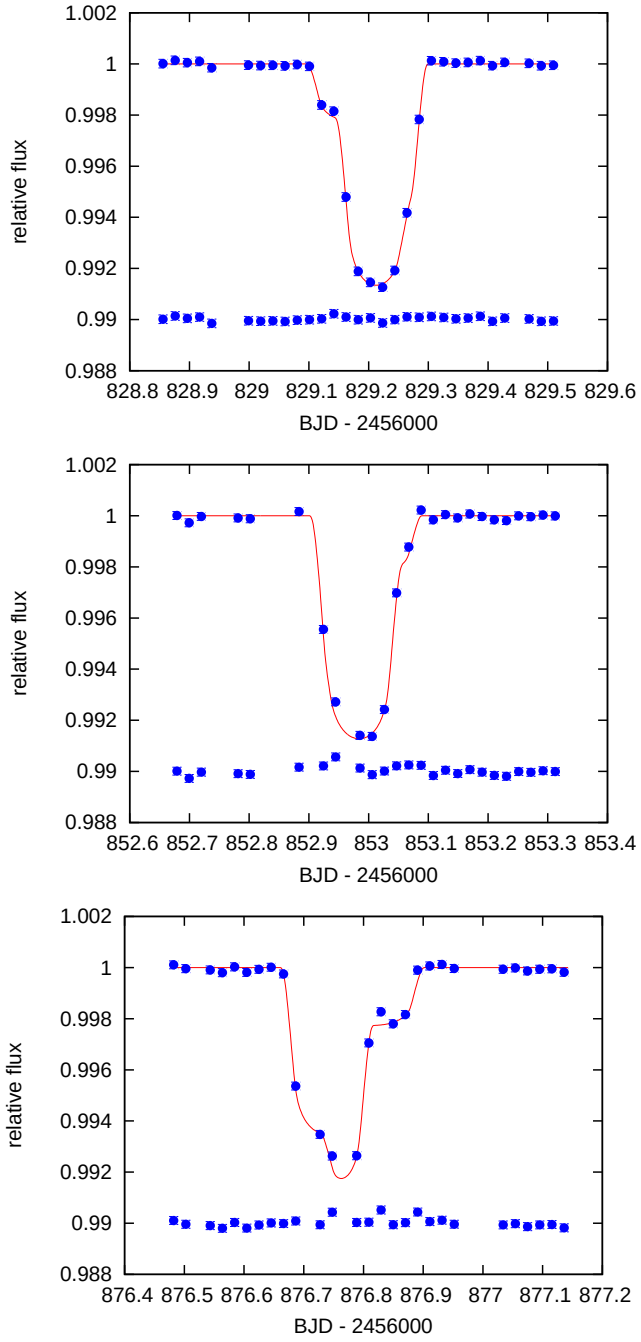

Fig. 3.— Mutual transit events observed in K2 data. Out-of-transit regions are normalized by the ESPRINT pipeline (Sanchis-Ojeda et al. 2015). Blue points show the light curve data and the red solid lines represent the best-fit models. Residuals are plotted with vertical offset by -0.01.

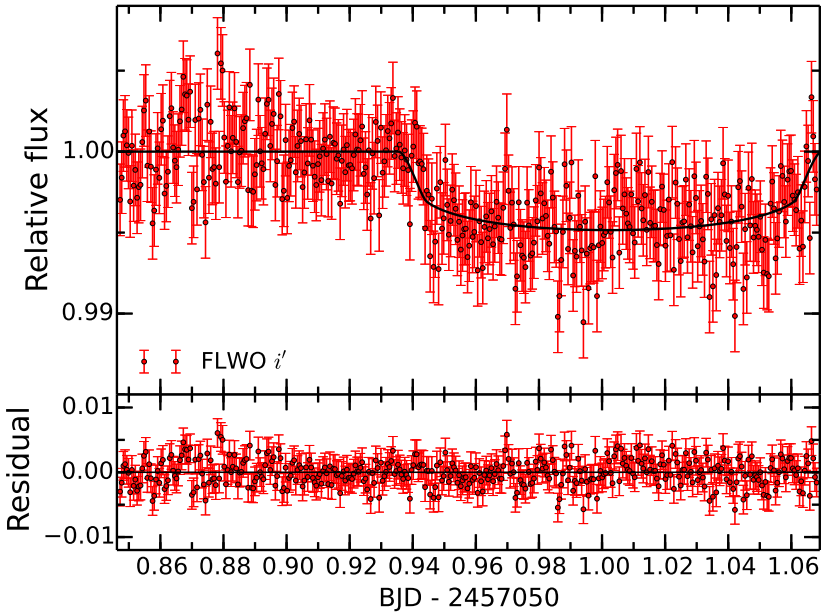

Fig. 4.— A transit light curve obtained with FLWO 1.2m telescope.

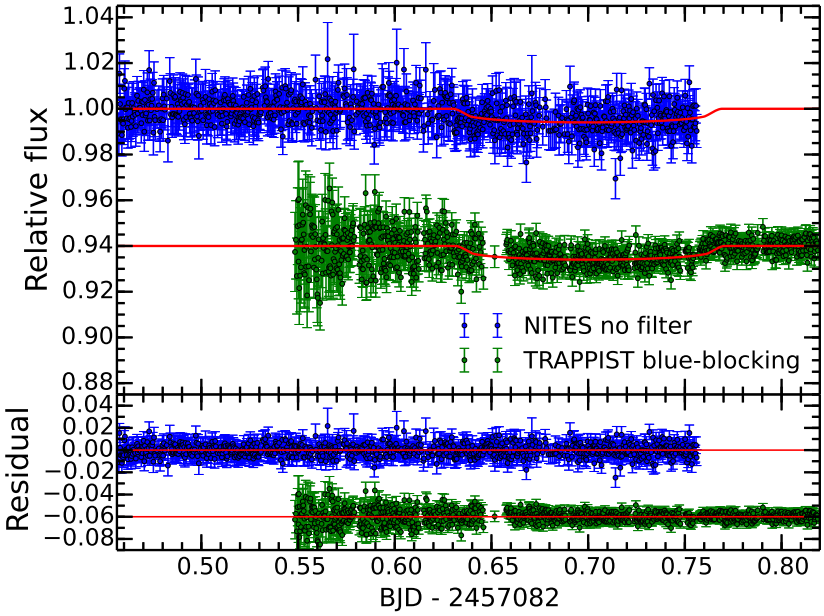

Fig. 5.— Transit light curves taken by TRAPPIST 0.6m and NITES 0.4m telescopes.

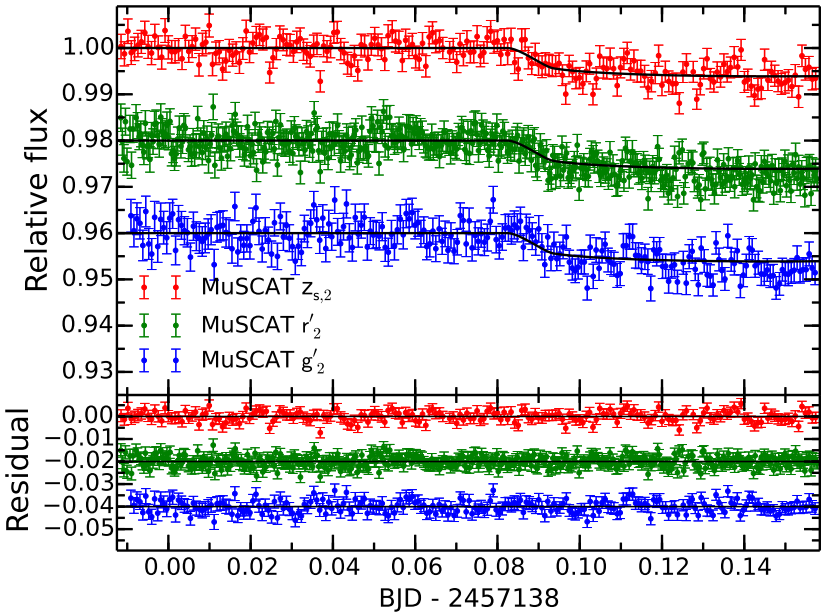

Fig. 6.— Same as Fig. 5, but by MuSCAT on OAO 1.88m telescope.

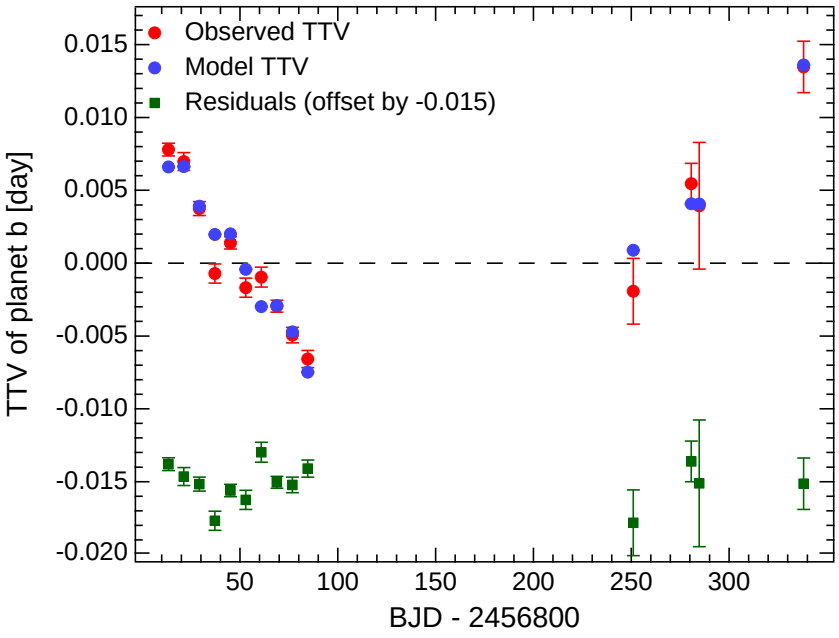

Fig. 7.— Observed TTV (red) and the minimum χ^2 model (blue) for the planet b. Residuals are plotted with vertical offset by -0.015. Data for TRAPPIST and NITES are plotted with horizontal offset by -2 and +2, respectively, for visual purpose.

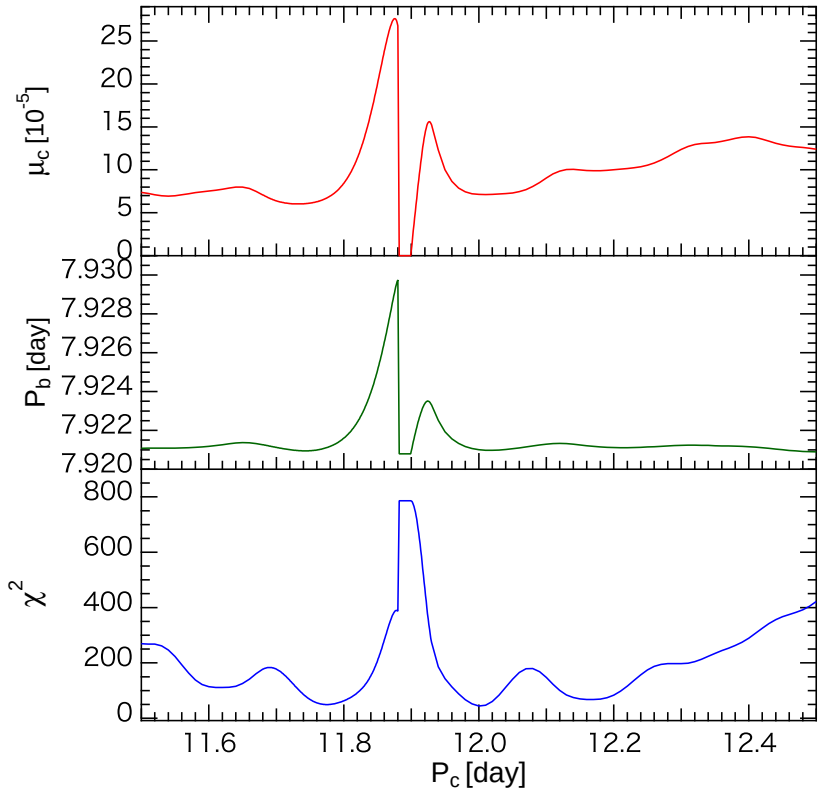

Fig. 8.— Variations of χ^2 (bottom) and optimal $P_{\rm b}$ (middle) and $\mu_{\rm c}$ (top) for $P_{\rm c}$ around the minimum χ^2 solution. The minimum χ^2 is located at $P_{\rm c} = 12.0028$, while the second-minimum one is placed at $P_{\rm c} = 11.7748$ with $\Delta\chi^2 = 5.4$. The difference of χ^2 is not statistically significant.

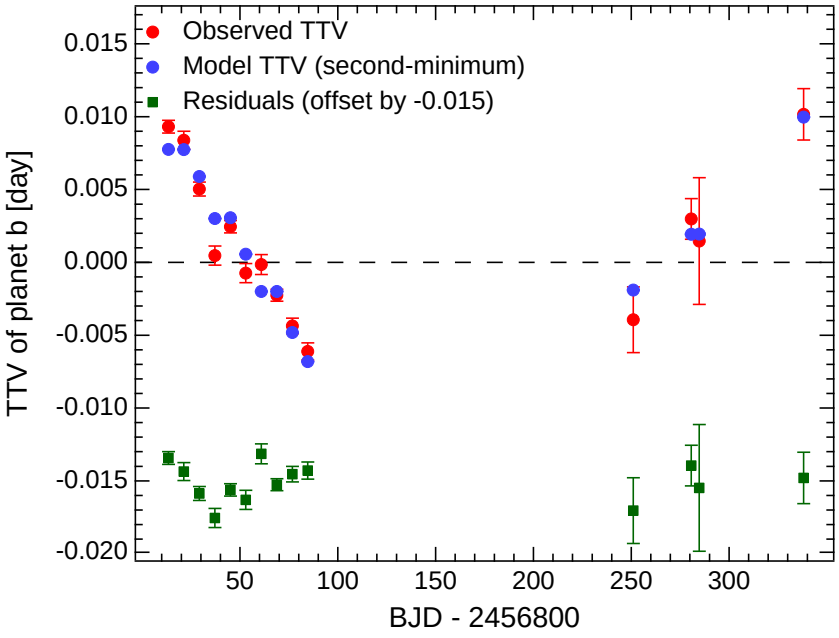

Fig. 9.— Same as Figure 7, but for the model for the second-minimum χ^2.

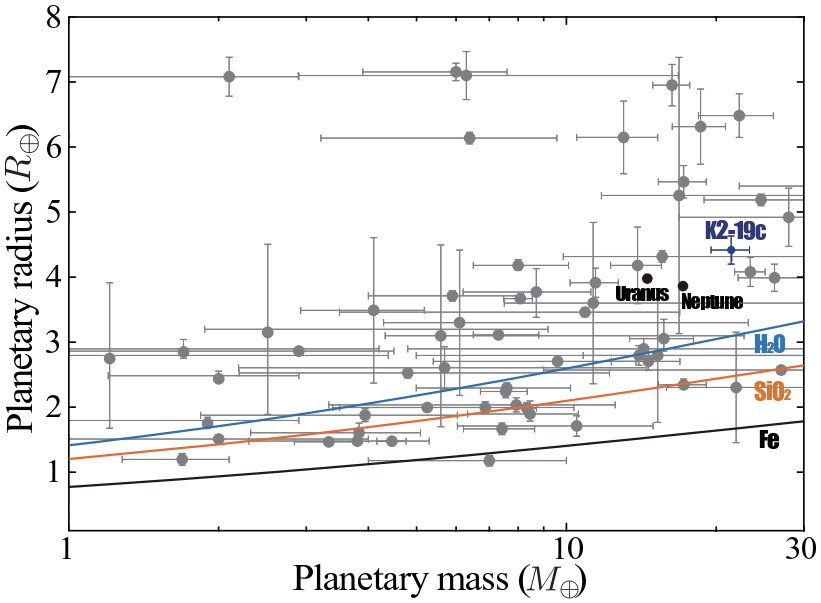

Fig. 10.— Mass-radius relationship of transiting planets. Theoretical mass-radius relations correspond to a pure water (blue), a silicate (orange), and an iron (black) planet (Zeng & Sasselov 2013). K2-19c with $21.4 \pm 1.9\,M_\oplus$ (see Table 5) and $4.37 \pm 0.22\,R_\oplus$ (see Table 2), which is larger than the radius of a pure water planet with the same mass, is likely to possess an atmosphere atop its core. Other data points shown in the figure are taken from the Exoplanet Orbit Database (Han et al. 2014).

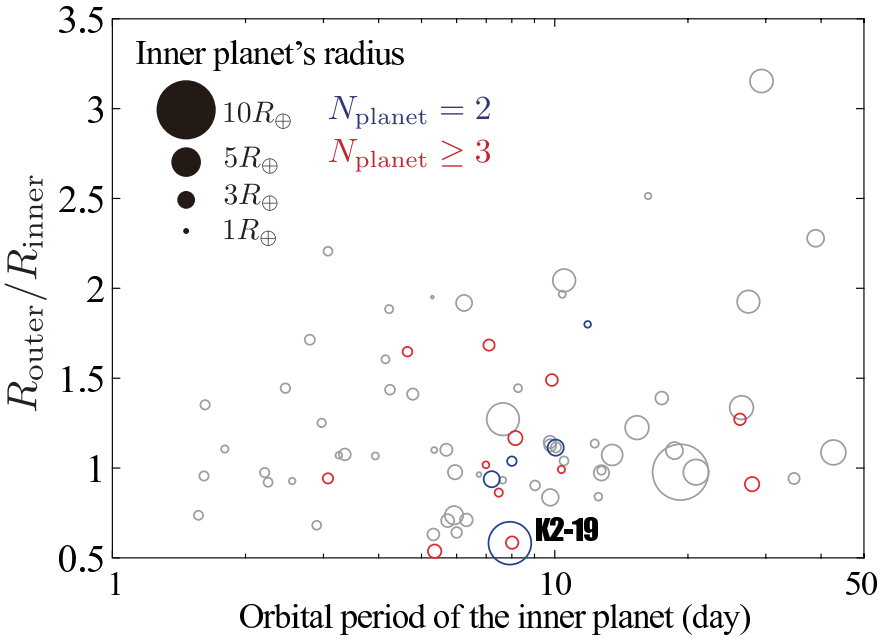

Fig. 11.— Radius ratio of a neighboring pair near or in a 3:2 MMR in multiple planet systems. The size of each circle is proportional to the radius of the inner planet. The multiplicity of a planetary system is shown by blue (2-planet) and red (≥ 3-planet) circles. We also plot a pair of planets close to a 2:1 commensurability in gray.

Table 1: Stellar parameters derived from high dispersion spectroscopy.

parameter	value	error[a]
$T_{\rm eff}$ [K]	5345	17
$\log g$	4.394	0.050
[Fe/H]	0.07	0.03
$R_{\rm s}$ [$R_\odot$]	0.914	0.027
$M_{\rm s}$ [$M_\odot$]	0.902	0.011
$V \sin I_{\rm s}$ [km s^{-1}]	0.85	$^{+0.95}_{-0.85}$
Age [Gyr]	≥ 8	–

[a]Presented errors are derived from statistical measurement errors in equivalent widths of iron lines. Additional systematic error (say, 40 K in $T_{\rm eff}$) may exist. Discussions on such systematic errors are presented in Hirano et al. (2014).

Table 2: Best fitting parameters and errors for K2 transit light curves. Derived planetary radii are also presented.

parameter	value	error
$a/R_{\rm s,b}$	19.35	$^{+0.56}_{-1.45}$
$a/R_{\rm s,c}$	24.09	$^{+1.72}_{-3.01}$
$b_{\rm b}$	0.233	$^{+0.213}_{-0.163}$
$b_{\rm c}$	0.367	$^{+0.260}_{-0.246}$
$R_{\rm p}/R_{\rm s,b}$	0.0737	$^{+0.0016}_{-0.0011}$
$R_{\rm p}/R_{\rm s,c}$	0.0439	$^{+0.0018}_{-0.0009}$
$T_{14,\rm b}$ [day]	0.1362	$^{+0.0020}_{-0.0014}$
$T_{14,\rm c}$ [day]	0.1536	$^{+0.0042}_{-0.0027}$
$u_1 + u_2$	0.69	$^{+0.18}_{-0.14}$
$u_1 - u_2$	0.06	$^{+0.35}_{-0.38}$
$R_{\rm p,b}$ [$R_\oplus$]	7.34	$\pm$0.27
$R_{\rm p,c}$ [$R_\oplus$]	4.37	$\pm$0.22

Table 3: A list of mid-transit times (T_c) for planet b and c from K2 transit light curves.

planet b				planet c			
epoch	T_c	error	β	epoch	T_c	error	β
0	2456813.38403	0.00044	1.00	0	2456817.27227	0.00144	1.00
1	2456821.30421	0.00061	1.00	1	2456829.18406	0.00170	1.12
2	2456829.22197	0.00048	1.12	2	2456841.09346	0.00198	1.30
3	2456837.13851	0.00066	1.00	3	2456853.00224	0.00214	1.03
4	2456845.06161	0.00042	1.00	4	2456864.90713	0.00127	1.00
5	2456852.97953	0.00066	1.03	5	2456876.81473	0.00135	1.04
6	2456860.90124	0.00068	1.00	6	2456888.71247	0.00191	1.00
7	2456868.82024	0.00041	1.00				
8	2456876.73925	0.00054	1.04				
9	2456884.65861	0.00059	1.00				

Table 4: Best fitting parameters and uncertainties for ground-based transit light curves.

	FLWO		TRAPPIST		NITES	
parameter	value	error	value	error	value	error
epoch	30		34		34	
T_c	2457051.00413	$^{+0.00218}_{-0.00225}$	2457082.69550	$^{+0.00140}_{-0.00116}$	2457082.69398	$^{+0.00342}_{-0.00435}$
R_p/R_s	0.0633	$^{+0.0042}_{-0.0045}$	0.0682	$^{+0.0043}_{-0.0046}$	0.0645	$^{+0.0082}_{-0.0109}$
i [deg]	90.00	$^{+0.80}_{-0.83}$	90.00	± 0.46	90.00	± 0.72
a/R_s	19.22	$^{+0.44}_{-0.56}$	19.58	$^{+0.30}_{-0.34}$	19.35	$^{+0.43}_{-1.12}$
k_0	0.9899	± 0.0025	1.0012	± 0.0017	0.9982	$^{+0.0011}_{-0.0013}$
k_t	-0.0077	± 0.0024	–		-0.0043	$^{+0.0031}_{-0.0035}$
k_z	0.00199	$^{+0.00075}_{-0.00079}$	-0.00020	$^{+0.00036}_{-0.00035}$	–	
$k_{\rm flip}$	–		-0.00030	$^{+0.00033}_{-0.00031}$	–	
β	1.258		1.000		1.000	

	MuSCAT(g'_2)		MuSCAT(r'_2)		MuSCAT($z_{s,2}$)	
parameter	value	error	value	error	value	error
epoch	–		41		–	
T_c	–		2457138.15047	$^{+0.00145}_{-0.00176}$	–	
R_p/R_s	0.0753	$^{+0.0067}_{-0.0070}$	0.0789	$^{+0.0043}_{-0.0041}$	0.0730	$^{+0.0058}_{-0.0061}$
i [deg]	–		88.94	$^{+0.73}_{-0.95}$	–	
a/Rs	–		18.80	$^{+0.94}_{-2.10}$	–	
k_0	0.9943	$^{+0.0046}_{-0.0047}$	0.9945	± 0.0028	0.9913	± 0.0040
k_t	-0.0243	$^{+0.0046}_{-0.0047}$	-0.0107	± 0.0027	-0.0095	± 0.0041
k_z	0.0014	± 0.0015	0.00188	± 0.00089	0.0030	± 0.0013
β	1.059		1.000		1.069	

Table 5: Planetary parameters derived by the TTV analysis. Coefficients for the synodic chopping formulae are also presented.

	minimum χ^2		second minimum χ^2	
parameter	value	error[a]	value	error[a]
$P_{\rm b}$ [day]	7.920994	0.000071	7.921122	0.000176
$P_{\rm c}$ [day]	12.0028	0.0092	11.7748	0.0142
$\mu_{\rm c}$	0.0000713	0.0000057	0.0000672	0.0000087
$T_c(0)_b$	2456813.37624	0.00050	2456813.37466	0.00109
χ^2/ν	43.98/10	–	49.38 / 10	–
$M_{\rm c}$	21.4	1.9	20.2	2.7
$P_{\rm c}/P_{\rm b}$	1.51531	0.00117	1.48651	0.00180
$f_b^{(1)}(\alpha)$	11.91	–	13.51	–
$f_b^{(2)}(\alpha)$	20.09	–	21.19	–
$f_b^{(3)}(\alpha)$	-139.71	–	178.84	–
$f_b^{(4)}(\alpha)$	-4.10	–	-5.56	–
$f_b^{(5)}(\alpha)$	-1.22	–	-1.57	–
$f_b^{(6)}(\alpha)$	-0.50	–	-0.64	–
$P_{\rm syn}$	23.29234	–	24.20293	–
α	0.75799	–	0.76776	–

[a]Presented errors are inflated by $\sqrt{\chi^2/\nu}$ to account for possible systematic errors.